Title	In Situ Activation of Anodized Ni-Fe Alloys for the Oxygen Evolution Reaction in Alkaline Media
Author(s)	Yamada, Naohito; Kitano, Sho; Yato, Yuya et al.
Citation	ACS applied energy materials, 3(12), 12316-12326 https://doi.org/10.1021/acsaem.0c02362
Issue Date	2020-12-28
Doc URL	https://hdl.handle.net/2115/83735
Rights	This document is the Accepted Manuscript version of a Published Work that appeared in final form in ACS applied energy materials, copyright c American Chemical Society after peer review and technical editing by the publisher. To access the final edited and published work see https://pubs.acs.org/doi/10.1021/acsaem.0c02362, see http://pubs.acs.org/page/policy/articlesonrequest/index.html.
Type	journal article
File Information	NiFe_OER_rev2.pdf

In-situ activation of anodized Ni-Fe alloys for the oxygen evolution reaction in alkaline media

Naohito Yamada,[†] *Sho Kitano,*[‡] *Yuya Yato,*[†] *Damian Kowalski,*[‡] *Yoshitaka Aoki,*[‡] *Hiroki Habazaki*[‡,]*

[†]Graduate School of Chemical Sciences and Engineering, Hokkaido University, Sapporo, Hokkaido 060-8628, Japan

[‡]Division of Applied Chemistry, Faculty of Engineering, Hokkaido University, Sapporo, Hokkaido 060-8628, Japan

Corresponding author: Phone & Fax +81-11-706-6575, e-mail habazaki@eng.hokudai.ac.jp

ABSTRACT

A simple anodizing technique has been employed to develop highly active electrocatalysts that can be applied to the oxygen evolution reaction (OER) in alkaline media. NiFe alloys were electrodeposited and anodized to form a porous electrocatalytic layer. This approach produces highly active electrodes without the need for noble metals, binders, or conductive carbon additives. The as-anodized electrode initially exhibits poor OER activity in 1.0 mol dm^{-3} KOH; however, the effects of potential cycling improve the OER activity to the extent that an overpotential as low as 0.26 V at 10 mA cm^{-2} is observed for the anodized Ni-11.8 at% Fe electrode. Although significant in-situ activation is achieved with anodized NiFe electrodes, this activation is less significant for as-deposited NiFe or anodized Ni electrodes. Furthermore, OER activity is observed to be composition dependent, with the Ni-11.8 at% Fe electrode exhibiting the greatest activity. A porous fluoride-rich, Fe-doped Ni oxyfluoride layer produced by anodizing is converted via potential cycling to an amorphous or poorly crystalline Fe-doped $Ni(OH)_2$ layer with a nanoflake-like morphology. The high activity is maintained even after almost removal of fluoride. Thus, the F-rich, Fe-doped Ni oxyfluoride is a promising precursor to develop a highly active OER electrode.

KEYWORDS: electrocatalysts, oxygen evolution reaction, anodizing, Ni-Fe alloy, porous anodic film

INTRODUCTION

Because of the limited availability of fossil fuels and pertinent global environmental issues, hydrogen production via electrochemical water splitting using renewable resources is an important alternative for future energy economies. Hydrogen is currently produced from oil, coal, and natural gas by processes that generate greenhouse gases as byproducts. Although hydrogen-based fuel cells are commercially available, this technology still uses fossil fuels to produce hydrogen. Thus, it is necessary to develop clean hydrogen production technologies based on renewable resources such as solar, wind, water, and biomass energies.[1]

An obstacle to the use of electrochemical water splitting for clean hydrogen production is the sluggish kinetics of the oxygen evolution reaction (OER). The large overpotential required to generate hydrogen and oxygen from water reduces the efficiency of converting electricity to hydrogen. Although the oxides of Ru and Ir are highly active and durable during OER,[2-3] their limited availability and high costs hinder their applicability for energy conversion and storage. Thus, extensive efforts have been directed toward the development of noble-metal-free electrocatalysts for the OER.

Transition metal oxides, oxyhydroxides, and hydroxides are promising candidates as OER electrocatalysts. Several strategies including nanostructuring and electronic structure control have been explored to enhance electrocatalytic activity. For example, Co oxide nanoparticles integrated into graphene and carbon nanotubes exhibit superior OER activity.[4-7] Strong coupling between transition metal oxides or hydroxides and nanocarbons in nanohybrids significantly improves electrocatalytic activity.[8-12] Transition metal oxides, spinel oxides,[13] and perovskite oxides[14] have attracted considerable attention as OER electrocatalysts. Transition metal hydroxides, layered double hydroxides (LDHs), and oxyhydroxides comprising first-row transition metals (Fe, Co, and Ni) have also attracted considerable interest in the last decade. A significant degree of OER activity has been demonstrated by nanosheets of $Ni(OH)_2$ and $Co(OH)_2$ and their oxyhydroxides.[15-18] Zhou et al. reported greatly enhanced OER performance using Fe-doped $Ni(OH)_2$ as compared to those of $Ni(OH)_2$ and NiFe LDH. [19] The improvement in activity is attributed to the enrichment of active surface sites, large defects, and enhanced surface wettability. Co-Fe LDH nanosheets with an increased number of defect sites and vacancies exhibit outstanding catalytic OER activity, which is characterized by an overpotential of 232 mV at 10 mA cm^{-2} and a Tafel slope of 36 mV per decade.[20]

Although highly active noble-metal-free electrocatalysts have been found for the OER, several issues must be addressed before utlizing these electrocatalysts for water splitting. Nanostructured electrocatalysts need to be coated on the current collector using polymer binders such as polytetrafluorethylene or Nafion. Inclusion of these binders inhibits mass transport due to the burying of catalytically active sites.[21-23] Transition metal oxides, hydroxides, and oxyhydroxides are typically poor conductors, and additives such as carbon black must be mixed with the electrocatalysts to impart suitable electronic conductivity.[24] However, corrosion of the carbon additives under OER conditions degrades the performance of the oxygen-generating anode.[25-27] In addition, the coated catalysts often peel off from the substrate during long-term electrolysis, particularly at high current densities.[28] Thus, conventional nanostructured electrocatalysts coated on current collectors with polymer binders and carbon additives do not meet the requirements of a practical OER anode for hydrogen production by water splitting.

Anodizing of metals and alloys is a promising means of directly fabricating an OER electrocatalyst on a metallic current collector. Fan et al. anodized an FeCoNi alloy in a fluoride-containing organic electrolyte to produce an amorphous oxide nanosheet on the alloy surface.[29]

They reported an extremely low overpotential of ~170 mV at 5 mA cm^{-2} for the OER using the anodized alloy. They also reported that crystallization of the amorphous oxide via heat treatment substantially increased the overpotential of the OER, thereby highlighting the importance of the amorphous nature of the oxide. Schäfer et al. employed a hard anodizing technique in KOH electrolyte to convert the surface of the AISI 304 stainless steel into a highly active NiFe-based oxide layer.[30] They reported an overpotential of 212 mV at 12 mA cm^{-2} in 1.0 mol dm^{-3} KOH. The same group anodized AISI Ni42 steel at a high current density in NaOH to form a 5-μm-thick porous oxide layer.[31] The anodized steel proved to be a good bifunctional electrocatalyst for the OER and hydrogen evolution reactions and exhibited good durability and better OER activity than those of IrO_2-RuO_2 in neutral and alkaline electrolytes. Steel-based electrocatalysts for water splitting are well summarized in a recent review.[32]

The electrodeposition and subsequent anodizing of alloys is an important approach for the direct fabrication of electrocatalysts. Dong et al. described the roll-to-roll fabrication of electrodeposited NiFe foils and subsequent anodizing to form highly active OER catalysts in an alkaline electrolyte.[33] These electrodes exhibited an overpotential of 251 mV at 10 mA cm^{-2} in 1.0 mol dm^{-3} KOH and prolonged stability. A porous Ni current collector was directly anodized in an organic electrolyte containing fluoride and various concentrations of $FeCl_2$ to form well-mixed NiFe oxides.[34] Park et al. combined an anodized NiFe OER electrode with an H_2-evolving NiMo electrode to split water in a perovskite/Si solar cell with a solar-to-hydrogen conversion exceeding 17%.[35] These studies suggest that anodizing is a very useful strategy for fabricating practical water-splitting anodes. However, the active species and factors that influence the activity and durability of anodically formed layers in the OER need to be further investigated.

In the present study, several compositions of NiFe alloys are electrodeposited onto a Ni substrate and anodized to form porous anodic films. The as-anodized specimens exhibit relatively low OER activity, but the activity significantly improves upon OER potential cycling. The overpotential becomes as low as 260 mV at 10 mA cm^{-2} in 1.0 mol dm^{-3} KOH after in-situ activation. Structural and compositional studies have also been conducted to characterize the active species and the activation mechanism of the anodized electrodes. Anodizing was conducted in a fluoride-containing ethylene glycol electrolyte to form a porous anodic layer. This electrolyte was selected because the formation of porous layer on Ni and Ni-base alloys was difficult in conventional aqueous electrolytes and fluoride-free organic electrolytes. Only fluoride-containing phosphoric acid or organic electrolytes have been used to form a porous anodic layer.[36-39]

2. EXPERIMENTAL

The substrate used for electrodeposition was a 0.3-mm thick 99% pure Ni plate (Nilaco Corp., Japan). The plate was cleaned ultrasonically in acetone, ethanol, and Milli-Q water prior to electrodeposition. The electrolyte compositions used for electrodeposition are summarized in Table 1. Electrodeposition was carried out at a constant cathodic current density of 50 mA cm^{-2} for 50 min at a bath temperature of 50 °C. The counter electrode was a Ni plate, and the distance between the two electrodes was 20 mm. The specimens were washed with Milli-Q water and dried in air after deposition.

Table 1. Compositions of the electrolytes used for electrodeposition.

Chemical	$NiSO_4 \cdot 6H_2O$	$FeSO_4 \cdot 7H_2O$	$NiCl_2$	H_3BO_3	Saccharin
Concentration (g dm^{-3})	43.37	0.46	3.63	30.0	5.0
	42.93	0.92			
	42.50	1.38			
	41.53	1.83			

The electrodeposited specimens were oxidized at 10 V in an ethylene glycol electrolyte containing 0.2 mol dm^{-3} NH_4F and 0.1 mol dm^{-3} H_2O for 12 h at room temperature to form nanoporous anodic films. A two-electrode electrochemical cell with a Pt counter electrode was used for anodizing. The specimens were washed in Milli-Q water and dried in air after anodizing.

The electrodeposited and anodized specimens were examined using a scanning electron microscope (SEM; Zeiss, Sigma-500) operating at 1.5 keV. Scanning transmission electron microscopy (STEM; JEOL, JEM-ARM200F) with EDS capability was used for cross-sectional observation and elemental analysis. Electron-transparent sections were prepared using a focused ion beam system (Hitachi, FB-2100). X-ray diffraction (XRD) measurements (Rigaku, RINT-2200) were performed to identify the phases in the electrodeposited and anodized specimens. An α-2θ mode with $\alpha = 2^{\circ}$ and a 2θ-range of 10–90° was used to enhance the sensitivity of reflections from the thin surface layer. The surface composition and chemical state of the elements and their depth profiles were examined using X-ray photoelectron spectroscopy (XPS; JEOL, JPS9010MC) with Mg K_{α} radiation ($h\nu = 1253.5$ eV). The area of the specimen analyzed was 3-mm in diameter. The binding energy was calibrated using the C 1s contaminant peak at

285.0 eV. Peak deconvolution was performed using the XPSPEAK41 software. Semi-quantitative compositional analysis was performed using the SpecSurf (JEOL) software.

Electrochemical experiments were conducted with a VersaSTAT 3 (Ametec Inc.) potentiostat/galvanostat system. OER performance was evaluated by cyclic voltammetry in 1.0 mol dm^{-3} KOH at room temperature using a three-electrode electrochemical cell with a Pt counter electrode and an Hg/HgO/1 mol dm^{-3} KOH reference electrode. The potential sweep rate was 10 mV s^{-1}. Polarization curves were recorded with 95% *iR* compensation. The *iR* drop was estimated via electrochemical impedance spectroscopy conducted at the open circuit potential with an AC amplitude of 10 mV and a frequency range of 100 kHz to 0.01 Hz. Cyclic voltammograms recorded at sweep rates of 10–140 mV s^{-1} between 0.74 and 0.88 V vs. RHE were used to estimate the electrochemical surface area (ECSA). The observed capacitance was converted to the ECSA using a specific capacitance of C_s = 0.020 mF cm^{-2}.[40-41]

3. RESULTS AND DISCUSSION

3.1. Characterization of alloy deposits

Figure 1a shows the correlation between the composition of the electrodeposited alloy and that of the electrodeposition bath. The Fe content of the alloy increases almost linearly with the Fe^{2+} concentration in the bath producing Ni-Fe alloys with compositions of 7.2–21.1 at% Fe. All deposits show similar XRD patterns (**Fig. 1b**), which are consistent with the fcc structure. The intensity ratios of the 111, 200, and 220 reflections suggest a random orientation of the deposited grains. The texture of the Ni substrate results in a very strong 200 reflection and a negligible 111 reflection, as shown in **Fig. 1b**. Cross-sectional SEM observations indicate the thickness of the deposits to be ~30 μm.

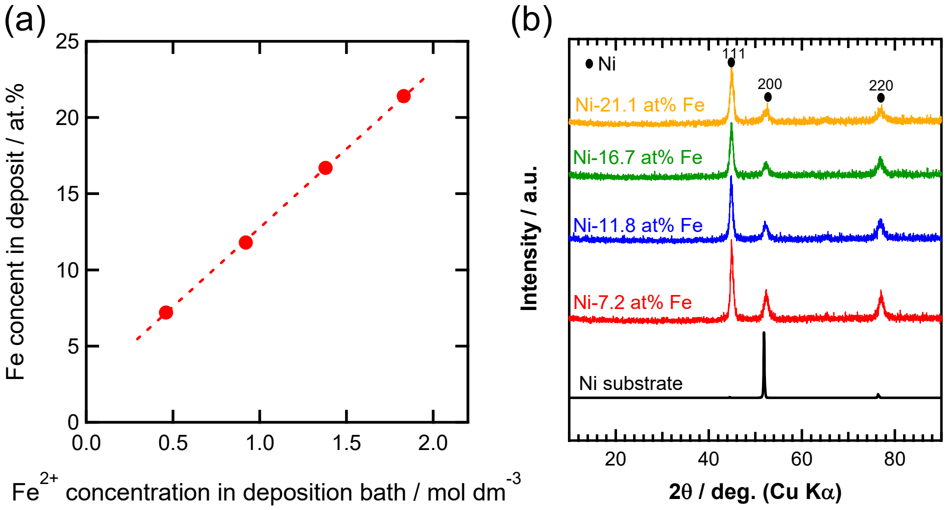

Figure 1. (a) Fe content of the deposit as a function of the Fe^{2+} concentration in the electrodeposition bath and (b) XRD patterns of the deposits and Ni substrate.

3.2. Characterization of anodic films

Figure 2 shows the current transients recorded during anodizing at a constant voltage of 10 V. The change in current density during anodizing is relatively small in all cases, and the current density decreases as the Fe content in the alloy increases. The current density at 16.7 at% Fe is nearly one-fifth of that of the Ni substrate. The surface changes appearance from metallic nickel to almost black after anodizing Ni and Ni-7.2 at% Fe, but Ni-11.8 at% Fe and Ni-16.7 at% Fe become gray in color after anodizing (**Fig. S1**). The change in color as a function of Fe content may be associated with the reduction in film thickness with greater Fe content, which is a consequence of the decrease in current density. The surface of the Ni-21 at% Fe sample is non-uniform in appearance, which suggests heterogeneous growth of the anodic film.

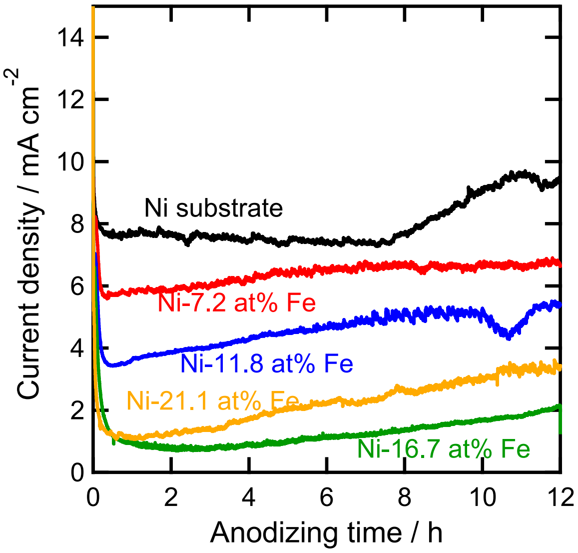

Figure 2. Current transients of NiFe deposits and Ni substrate during anodizing at 10 V in ethylene glycol containing 0.2 mol dm^{-3} NH_4F and 0.1 mol dm^{-3} H_2O for 12 h.

The surfaces of the anodized alloy deposits were examined using SEM (**Fig. 3**). Porous layers appear to be formed, but the pore sizes are rather small (<20 nm). Pore size is known to depend on the anodizing voltage in the formation of porous alumina and nanotubular titania films.[42-43] The use of a relatively low anodizing voltage (10 V) likely contributes to the formation of films with small pores. The porous nature of the films is more apparent in cross-section transmission electron micrographs. As an example, cross-sectional scanning transmission electron micrographs (BF-STEM and HAADF-STEM) of anodized Ni-11.8 at% Fe are shown in **Fig. 4**. The BF-STEM image (**Fig. 4a**) reveals the formation of an anodic film on the alloy deposit, which appears at the bottom of the micrograph. The anodic film has an irregular alloy/film interface, whereas the film surface is relatively smooth. Thus, the film thickness is not uniform. Non-uniform film growth is further evident from the lower magnification image shown in **Fig. S2**. Non-uniform film growth is unusual in the anodizing of metals and alloys, and further investigation is required to understand the reason for this behavior. The porous nature of the anodic film is obvious in **Fig. 4**, particularly from the HAADF-STEM image (**Fig. 4b**). The dark pores in **Fig. 4b** are larger in the inner part of the film as compared to those in the outer region of ~50 nm thickness. The selected area electron diffraction (SAED) pattern of the anodic film (**Fig. 4c**) reveals its crystalline nature and suggests the presence of a NiF_2 phase with the fluorite structure. The high-resolution image in **Fig. 4d** reveals the presence of nanocrystals, and the lattice fringe spacing of 0.33 nm corresponds to the (111) plane of NiF_2.

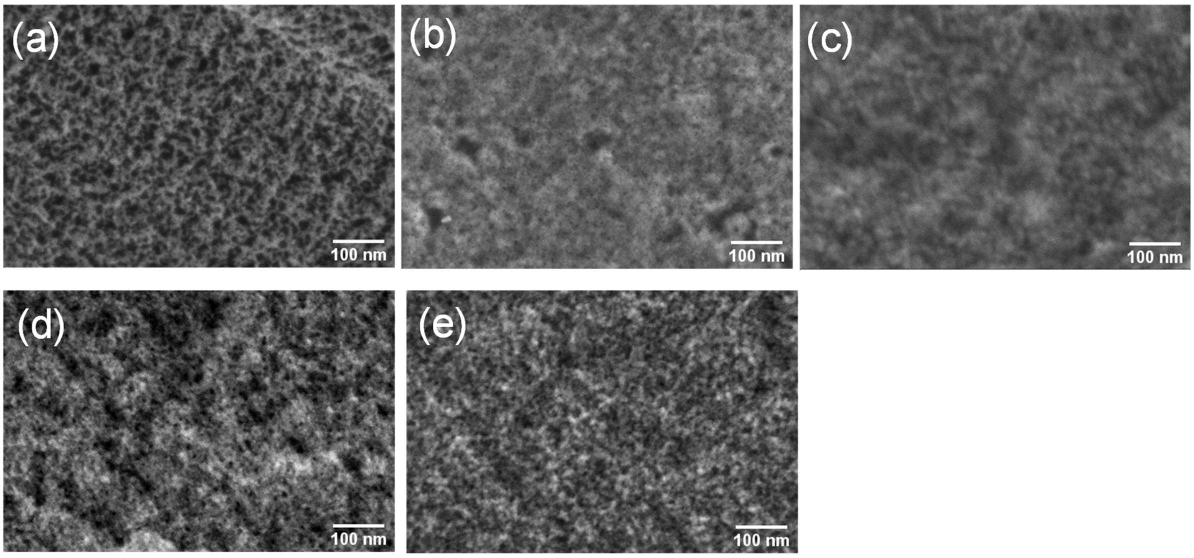

Figure 3. Scanning electron micrographs of (a) Ni substrate and electrodeposited (b) Ni-7.2 at% Fe, (c) Ni-11.8 at% Fe, (d) Ni-16.7 at% Fe and (e) Ni-21.1 at% Fe film surfaces prepared by 12-h anodizing at 10 V in ethylene glycol containing 0.2 mol dm^{-3} NH_4F and 0.1 mol dm^{-3} H_2O.

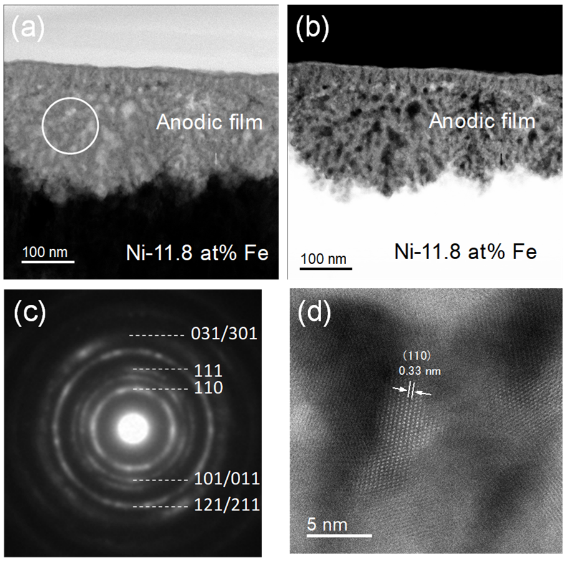

Figure 4. (a) BF and (b) HAADF scanning transmission electron micrographs, (c) selected-area electron diffraction pattern, and (d) high-resolution image in the anodic film region of Ni-11.8 at% Fe anodized at 10 V in ethylene glycol containing 0.2 mol dm^{-3} NH_4F and 0.1 mol dm^{-3} H_2O for 12 h.

Figure 5 shows EDS elemental mapping of anodized Ni-11.8 at% Fe. Ni and Fe are distributed uniformly throughout the film, and fluorine and oxygen are incorporated in the film. The quantitative analysis of regions 1-3 identified in **Fig. 5a** is summarized in **Table 2**. The three regions have similar compositions, and the Ni to Fe ratio is comparable to that of the alloy. The EDS analysis confirms the presence of a relatively high concentration of fluorine, which is more than twice greater than that of oxygen. Thus, the anodic films consist of fluoride-rich Ni oxyfluoride doped with Fe.

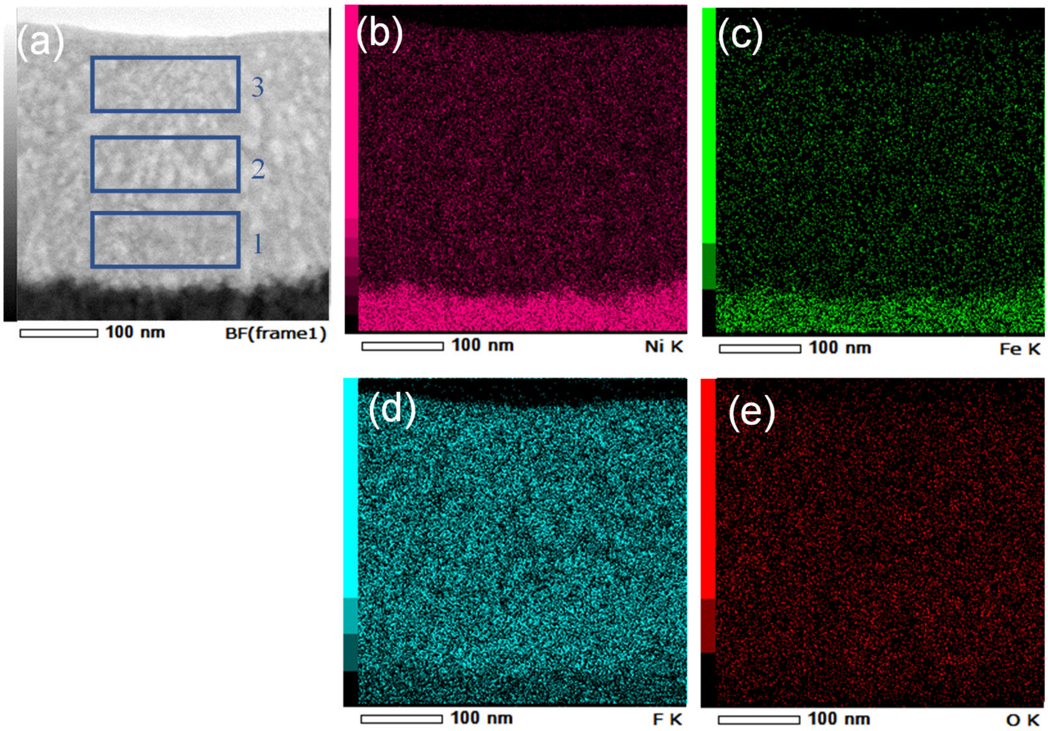

Figure 5. (a) BF-scanning transmission electron micrograph indicating the location of regions 1–3. EDS elemental mapping images of (b) Ni, (c) Fe, (d) F and (e) O in Ni-11.8 at% Fe anodized at 10 V in ethylene glycol containing 0.2 mol dm^{-3} NH_4F and 0.1 mol dm^{-3} H_2O for 12 h.

Table 2. Quantitative STEM-EDS analysis of regions 1–3 shown in Fig. 5a.

Element	Composition (at%)		
	Region 1	Region 2	Region 3
Ni	15.2	15.3	13.0
Fe	2.6	2.5	2.1
F	57.6	56.8	58.5
O	24.6	25.5	26.4

3.3. OER characteristics

The OER activity of the anodized alloy deposits was examined via cyclic voltammetry (CV). The CV curves of the anodized electrodes (**Fig. 6**) reveal that the initial OER activity of all the specimens is rather low; however, the OER current increases significantly during potential cycling. The enhancement in activity is greater for the anodized NiFe electrodes than that for the anodized Ni substrate. In contrast, the CV curves of as-deposited Ni-11.8 at% Fe (**Fig. S3**) show limited enhancement of OER activity during potential cycling. Thus, in-situ activation of the OER is characteristic of the anodized NiFe electrodes. A Ni^{2+}/Ni^{3+} redox couple is observed between 1.1 and 1.5 V in the CV curves of the anodized electrodes (**Fig. 6**). These redox peaks increase with potential cycling, which suggests a correlation between the redox activity and OER active sites. The Ni^{2+}/Ni^{3+} peaks are absent from the CV curves of as-deposited NiFe (**Fig. S3**), indicating that the redox-active sites are present in the porous anodic films.

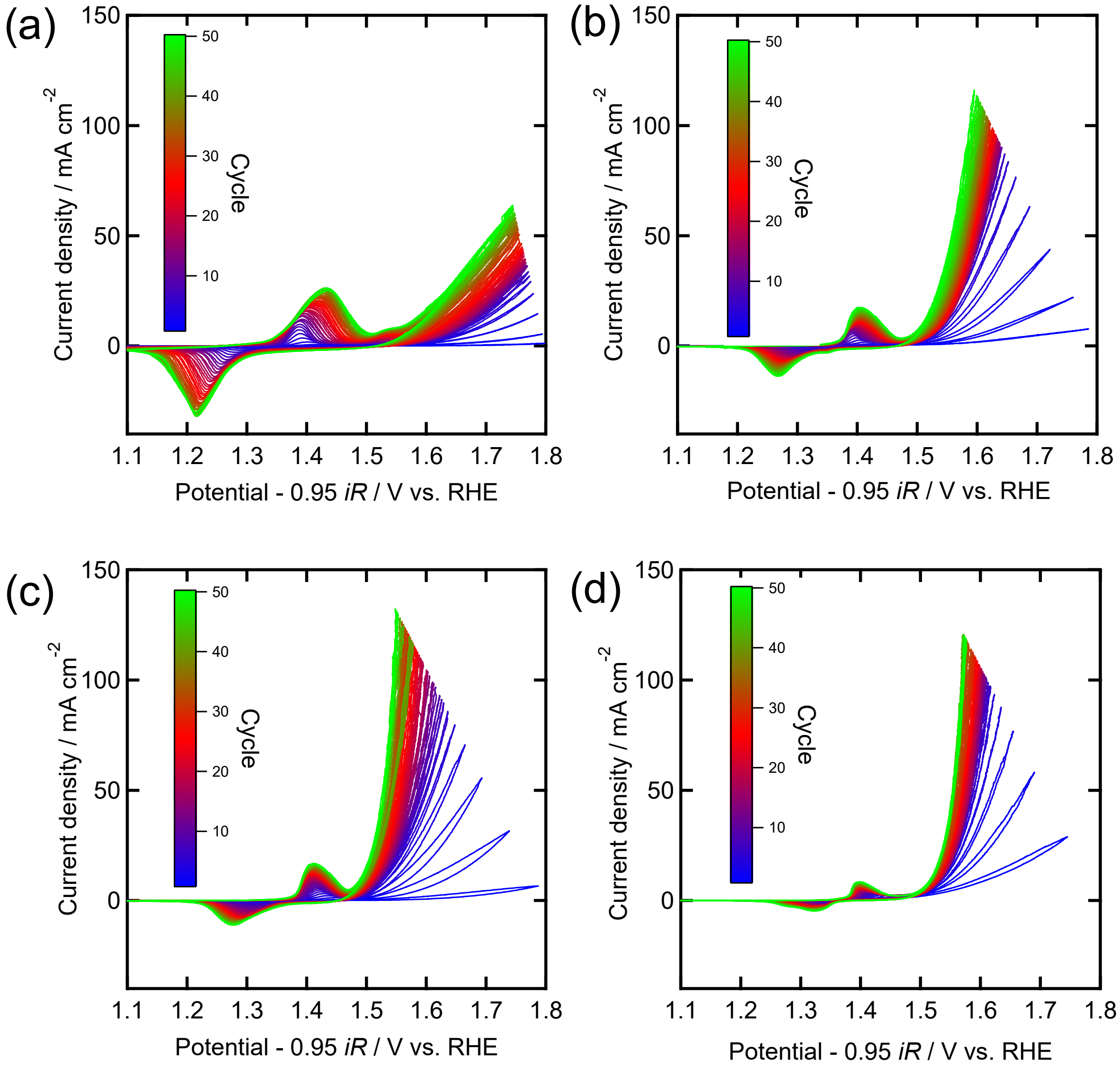

Figure 6. CV curves in 1.0 mol dm^{-3} KOH of (a) Ni substrate and electrodeposited (b) Ni-7.2 at% Fe, (c) Ni-11.8 at% Fe, and (d) Ni-16.7 at% Fe anodized at 10 V in ethylene glycol containing 0.2 mol dm^{-3} NH_4F and 0.1 mol dm^{-3} H_2O for 12 h.

Figure 7 compares the OER activity of the anodized electrodes after in-situ activation. The NiFe electrodes exhibit significantly greater OER activity than the Ni substrate (**Fig. 7a**). The addition of Fe to Ni enhances the OER performance. The best results are observed for Ni-11.8 at%

Fe, which is similar to the results of a recent study.[44] The Tafel slopes of the activated NiFe electrodes are similar to those of the Ni substrate without anodizing (**Fig. 7b**). Only anodized Ni exhibits a larger Tafel slope. The Tafel slopes are summarized in **Table 3**. The Tafel slopes of the anodized NiFe electrodes are similar to those of the electrochemically deposited Ni-Fe oxyhydroxide.[45] However, the absence of a composition dependence in the Tafel slopes contrasts with the results reported by Liang et al.,[44] which show the Tafel slopes of anodized NiFe electrodes to vary between 38 and 96 mV per decade as a function of alloy composition. The difference in behavior arises possibly from differences in the anodizing conditions used in the two studies. The CV curves and Tafel plots of activated Ni-11.8 at% Fe with and without anodizing are compared in **Fig. S4**. The much smaller overpotential produced by anodizing is evident from the CV curves. Thus, anodizing makes a very important contribution to the enhancement of OER activity in the NiFe deposits. However, the small changes in Tafel slope suggest that the rate-determining step is unchanged by anodizing. There are several reports showing the enhancing OER activity of Ni oxides, oxyhydroxides and hydroxides by the addition of Fe, but the role of Fe in enhancing the OER activity in alkaline media is still controversial; several proposed mechanisms are well summarized in a recent review.[46]

Table 3. Electrochemical characteristics of the NiFe deposits in KOH electrolyte.

	Alloy	η_{10} (V)	Tafel slope (mV decade^{-1})	ECSA before activation (cm^2)	ECSA after activation (cm^2)
Anodized	Ni	0.34	137	0.63	1.86
	Ni-7.2 at% Fe	0.28	61	0.59	2.08
	Ni-11.8 at% Fe	0.26	53	0.33	1.70

	Ni-16.7 at% Fe	0.29	53	0.50	1.77
	Ni-21.1 at% Fe	0.29	73	0.04	0.71
As-received	Ni	0.35	50	-	-
	Ni-11.8 at% Fe	0.38	52	0.85	2.51

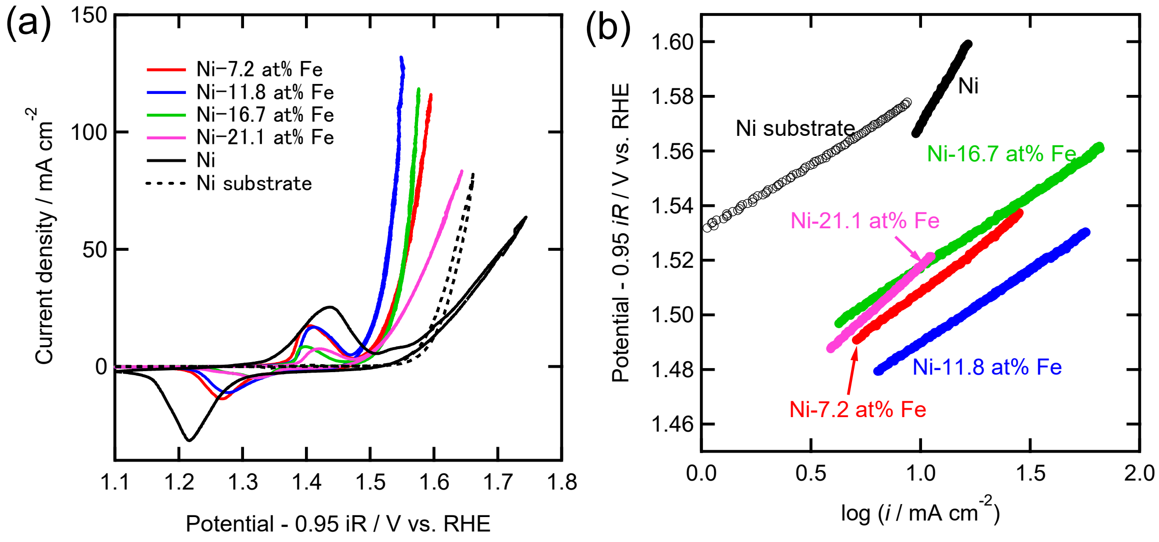

Figure 7. (a) CV curves and (b) Tafel plots of the anodized NiFe deposits and Ni substrate after in-situ activation using 50 CV cycles in 1.0 mol dm^{-3} KOH.

3.4. Mechanism of in-situ activation

To gain insights into the mechanism of in-situ OER activation on anodized NiFe electrodes, the electrochemical surface area (ECSA) was estimated from CV measurements in a potential range where no Faradaic reaction occurs.[41] Typical CV curves at several sweep rates are shown in **Fig. S5a** and **S5b**. There is a linear correlation between the current density at 0.84 V vs. RHE and the potential sweep rate (**Fig. S5c** and **S5d**). The double layer capacitance and ECSA were determined from the slope. The ECSA values of anodized NiFe electrodes before and after in-situ activation are listed in **Table 3**. The ECSA values of the anodized NiFe electrodes before and after activation are comparable to or smaller than that of anodized Ni. Thus, the greater OER activity of the Fe-containing electrodes is not due to an increase in the active surface area.

Additional factors may contribute to the enhancement of OER activity, because in-situ activation increases the OER current by more than one order of magnitude (**Fig. 6**). The compositional change in the surface after activation was examined by XPS. **Figure S6** shows wide-scan XPS spectra of anodized Ni-11.8 at% Fe before and after in-situ activation. Peaks for O and F are present in the as-anodized specimen in addition to the peaks for Ni and Fe. The intensity of the F 1s peak is much greater than that of the O 1s peak, which suggests that fluoride is the major anion on the anodized surface; this result is in agreement with the STEM/EDS analysis (**Table 2**). However, the F 1s peak disappears, and the intensity of O 1s peak increases after in-situ activation. Thus, in-situ activation significantly alters the surface composition. **Figure 8** shows narrow-scan Ni 2p, Fe $2p_{3/2}$, O 1s, and F 1s XPS spectra of the same specimens. The binding energy of the Ni $2p_{3/2}$ peak shifts from 856.8 to 855.5 eV upon activation. The latter value is close to the binding energy of $Ni(OH)_2$.[47] The greater binding energy before activation is attributed to the presence of fluoride, because the reported NiF_2 binding energy is 857.4 eV.[48] Activation also shifts the Fe $2p_{3/2}$ peak to a more negative energy. The 711.0 eV value after activation suggests the presence of Fe^{3+} on the activated surface.[49] The O 1s spectrum of the activated electrode shows a peak at 531.2 eV, which corresponds to OH-type oxygen[47] and suggests that a metal hydroxide is the principal component after activation. The F 1s spectrum indicates the almost complete absence of fluoride at the porous electrode surface after activation. Thus, Fe-doped, F-rich Ni oxyfluoride is converted into Fe-doped Ni hydroxide on the porous electrode surface during potential cycling in KOH electrolyte. **Table 4** summarizes the surface composition of as-anodized and in-situ activated Ni-11.8 at% Fe. The Fe to Ni ratio in the as-anodized electrode is similar to that observed in the alloy, and the F/Ni ratio of ≈2 indicates a principal composition of NiF_2, which is in agreement with the SAED pattern **(Fig. 3c**). The Fe to Ni ratio is almost unchanged by activation; however, the high oxygen content suggests the presence of hydrated Fe-doped $Ni(OH)_2$ on the activated surface.

Table 4. Surface composition of as-anodized and in-situ activated Ni-11.8 at% Fe determined using XPS.

Element	Composition (at%)			
	Ni	Fe	O	F
As-anodized	29.7	5.0	5.7	59.6
In-situ activated	16.4	2.3	79.7	1.6

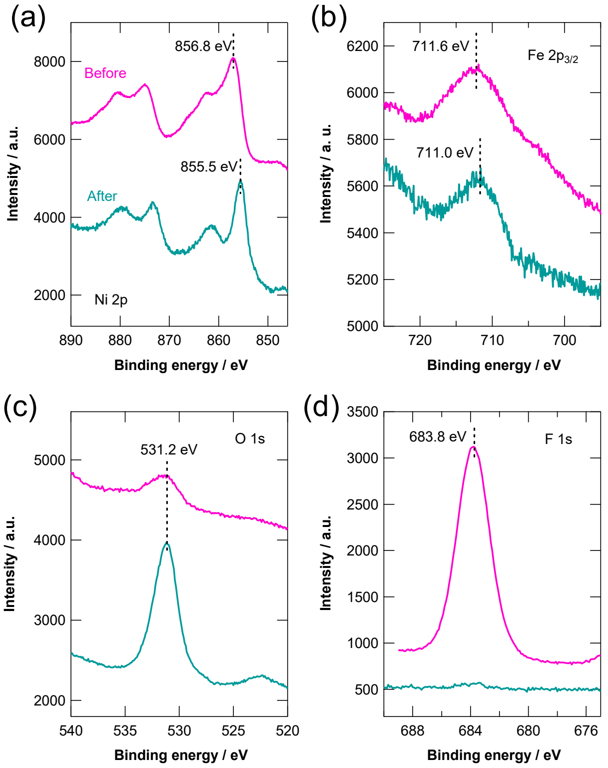

Figure 8. (a) Ni 2p, (b) Fe $2p_{3/2}$, (c) O 1s and (d) F 1s XPS spectra of as-anodized (purple) and in-situ activated (blue) Ni-11.8 at% Fe.

The in-situ activated electrode was further examined by STEM/EDS analysis and SEM observation. **Figure 9** shows a scanning electron micrograph of the surface and a cross-sectional BF-STEM image of in-situ activated Ni-11.8 at% Fe. The surface appearance after activation tends to change when compared to that of the as-anodized electrode (**Fig. 3**), and a nanoflake-like morphology develops. The flake-like morphology is typical of $Ni(OH)_2$.[50] The cross-sectional scanning transmission electron micrograph reveals that the thickness of the porous layer formed by anodizing is reduced to ~50 nm via in-situ activation. Dissolution of Ni and Fe species is apparently involved in the formation of the active constituent during transformation of the F-rich Ni oxyfluoride to the $Ni(OH)_2$-based material. The selected area electron diffraction pattern of the activated layer (**Fig. 9b**) reveals the absence of a highly crystalline phase. Thus, poorly crystalline or amorphous Fe-doped $Ni(OH)_2$ is primarily present in the activated electrode.

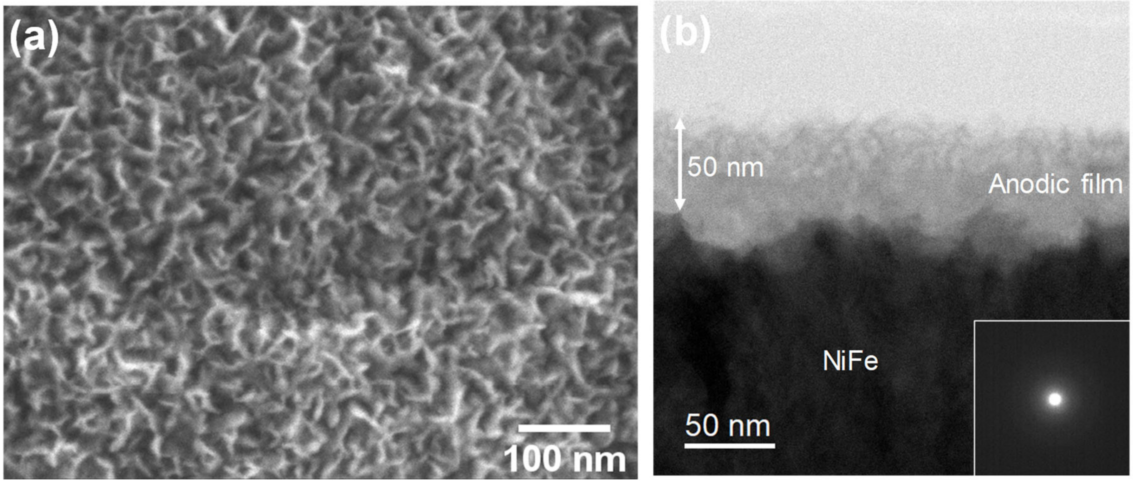

Figure 9. (a) Scanning electron micrograph and (b) scanning transmission electron micrograph and SAED of anodized Ni-11.8 at% Fe after in-situ activation in 1.0 mol dm^{-3} KOH via potential cycling.

STEM/EDS analysis of the cross-section of activated Ni-11.8 at% Fe (**Fig. 10**) shows a relatively uniform distribution of Ni and Fe in the hydroxide layer. Although fluorine is negligibly present on the surface, as shown in the XPS analysis (**Table 4**), it is clearly detected in the inner part of the hydroxide layer. The reduced fluorine content in the outer part of the hydroxide layer is evident upon comparing the O and Fe elemental maps (**Fig. 10d** and **10e**). The inner part of the porous electrode (**Fig. 10f**) contains 14 at% fluorine. Pei et al. reported that fluoridated Fe-Ni LDH exhibits greatly enhanced OER performance compared with that of pristine Fe-Ni LDH; further, they attributed the enhanced performance to the formation of a core-shell structure of Fe-doped high-valence Ni-oxyhydroxide over Fe-Ni fluoride.[51]

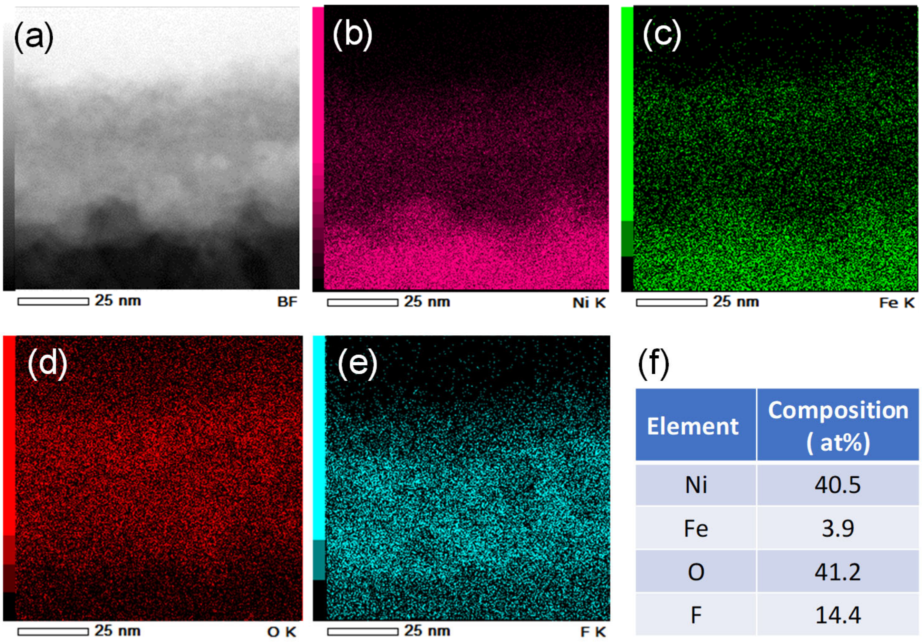

Element	Composition (at%)
Ni	40.5
Fe	3.9
O	41.2
F	14.4

Figure 10. (a) BF-scanning transmission electron micrograph and the corresponding EDS mapping images of (b) Ni, (c) Fe, (d) O and (e) F in anodized Ni-11.8 at% Fe after in-situ activation in 1.0 mol dm^{-3} KOH via potential cycling.

Prolonged oxygen evolution was conducted at a constant current density of 50 mA cm^{-2} to elucidate the role of the inner fluoride-containing layer in the OER performance. The constant potential of ~1.55 V vs. RHE maintained for 24 h during galvanostatic polarization (**Fig. 11a**) demonstrates the high stability of anodized Ni-11.8 at% Fe during OER. The flake-like surface morphology remains almost unchanged even after the durability test (**Fig. 11b**). The change in composition of the porous film on the alloy deposit after a 24-h OER was examined via the XPS depth profile analysis (**Fig. 11c–e**). The as-anodized deposit is rich in fluoride throughout the film. The oxygen content is low, except at the film surface. The fluoride content is reduced from 60 to 20 at% upon in-situ activation via potential cycling and conversion to the oxide-based porous layer. The fluoride content decreases further to less than a few at% after OER at 50 mA cm^{-2} for 24 h, although the high OER activity remains unchanged. The findings suggest that fluoride-containing moieties are not the primary active species in the OER, because substantial activity remains after removal of fluorine from the porous film. The active species appears to be the amorphous or poorly crystalline Fe-doped Ni hydroxide.

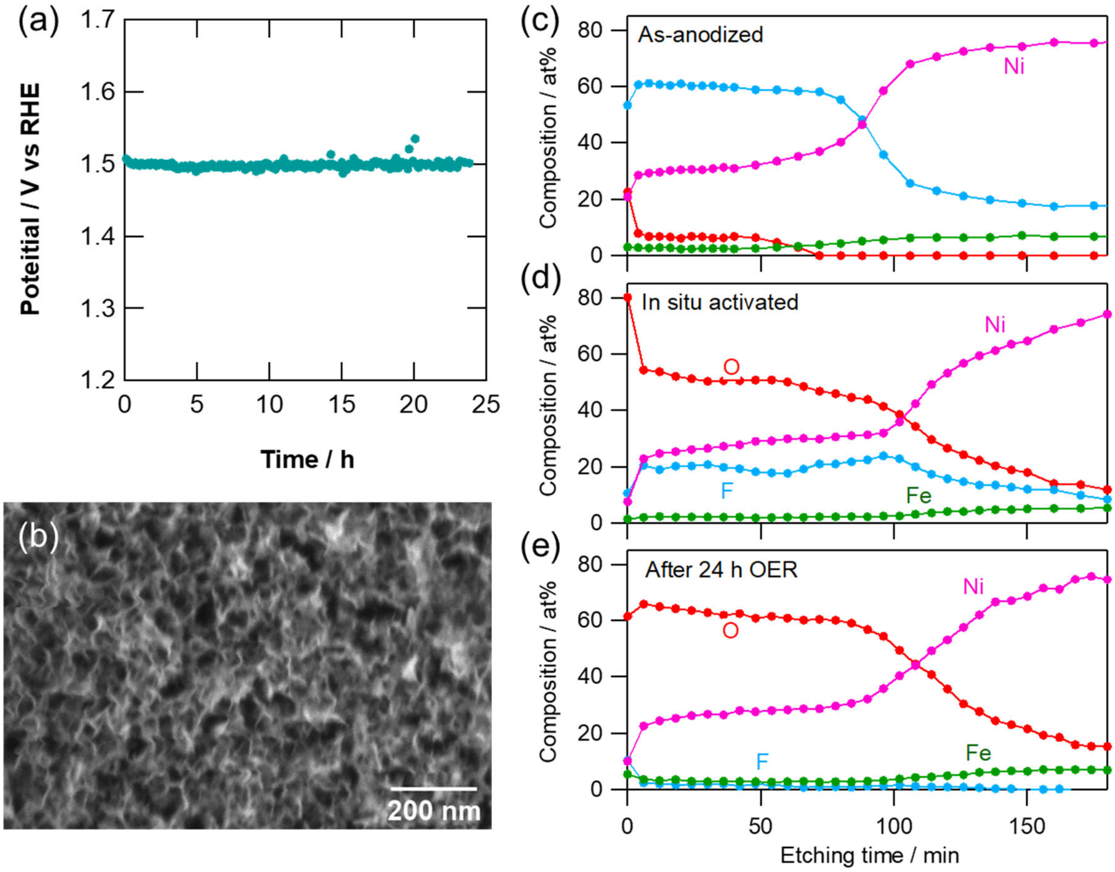

Figure 11. (a) Potential change of anodized and in-situ activated Ni-11.8 at% during durability testing at 50 mA cm^{-2} in 1.0 mol dm^{-3} KOH and (b) scanning electron micrograph of surface after the durability test. XPS depth profiles of Ni-11.8 at% Fe (c) as-anodized, (d) in-situ activated, and (e) after a 24-h durability test.

A substantial degree of OER activity is achieved during oxygen evolution at the anodized NiFe deposits. The activity enhancement is less significant during the potential cycling of the NiFe deposits without anodizing (**Fig. S3**), and the OER activity of the anodized NiFe deposit is remarkably higher than the as-anodized counterpart after potential cycling (Fig. S4a). Anodizing of the NiFe deposits forms porous F-rich oxyfluoride films, which are promising precursors of OER-active hydroxides. Such a porous hydroxide layer cannot be formed without anodizing of the NiFe deposits. Thus, only the anodized NiFe deposits exhibit marked activation for OER during potential cycling. The ejection of fluoride ions into alkaline aqueous electrolyte from the porous anodic layer promotes the formation of amorphous Fe-doped Ni hydroxide porous layer. This investigation describes a straightforward approach for fabricating highly active OER electrodes without using binder and conductive additives, via simple anodizing of electrodeposited NiFe electrodes.

4. CONCLUSIONS

The present study demonstrates the formation of highly active and durable OER electrodes via in-situ activation of anodized NiFe deposits. OER-active amorphous or poorly crystalline Fe-doped Ni hydroxide films are produced by the transformation of a porous fluoride-based layer during OER. The OER overpotential is as low as 0.26 V at 10 mA cm^{-2} in 1.0 mol dm^{-3} KOH. The fluoride content of the porous layer decreases during in-situ activation and becomes negligible after prolonged OER polarization, while the OER activity remains unchanged. Thus, fluoride-containing entities are not actively involved in the OER, but are effective precursors in the development of active species. These highly active OER electrodes are obtained via simple and cost-effective anodizing of electrodeposited NiFe alloys in a fluoride-containing organic electrolyte. No binder or conductive additives are needed to achieve high OER activity.

ASSOCIATED CONTENT

Supporting Information

The supporting information is available free of charge at https://pubs.acs.org/doi/

Additional characterization data (anodized specimen photographs, HAADF-STEM), additional electrochemical data (CV for OER, Tafel plots, CV for ECSA) (PDF)

AUTHOR INFORMATION

Corresponding Author

Hiroki Habazaki, Division of Applied Chemistry, Faculty of Engineering, Hokkaido University, Sapporo, Hokkaido 060-8628, Japan; orcid.org/0000-0002-7172-8811; e-mail: habazaki@eng.hokudai.ac.jp

Authors

Naohito Yamada – *Graduate School of Chemical Sciences and Engineering, Hokkaido University, Sapporo, Hokkaido 060-8628, Japan*

Sho Kitano – *Division of Applied Chemistry, faculty of Engineering, Hokkaido University, Sapporo, Hokkaido 060-8628, Japan*

Yuya Yato – *Graduate School of Chemical Sciences and Engineering, Hokkaido University, Sapporo, Hokkaido 060-8628, Japan*

Damian Kowalski – *Division of Applied Chemistry, faculty of Engineering, Hokkaido University, Sapporo, Hokkaido 060-8628, Japan*

Yoshitaka Aoki – *Division of Applied Chemistry, faculty of Engineering, Hokkaido University, Sapporo, Hokkaido 060-8628, Japan*

Notes

The authors declare no competing financial interest.

ACKNOWLEDGMENT

The present study was supported in part by JSPS KAKENHI (Grant Number 19H02469). A part of this work was conducted at the Promotion Office for the Nanotechnology Collaboration and Laboratory of XPS analysis, Hokkaido University, supported by "Nanotechnology Platform" Program of the Ministry of Education, Culture, Sports, Science and Technology (MEXT), Japan.

REFERENCES

1. Dincer, I.; Acar, C., Review and evaluation of hydrogen production methods for better sustainability. *Int. J. Hydrogen Energy* **2015,** *40* (34), 11094-11111.

2. Yu, J.; He, Q.; Yang, G.; Zhou, W.; Shao, Z.; Ni, M., Recent Advances and Prospective in Ruthenium-Based Materials for Electrochemical Water Splitting. *ACS Catalysis* **2019,** *9* (11), 9973-10011.

3. Wang, C.; Lan, F.; He, Z.; Xie, X.; Zhao, Y.; Hou, H.; Guo, L.; Murugadoss, V.; Liu, H.; Shao, Q.; Gao, Q.; Ding, T.; Wei, R.; Guo, Z., Iridium-Based Catalysts for Solid Polymer Electrolyte Electrocatalytic Water Splitting. *ChemSusChem* **2019,** *12* (8), 1576-1590.

4. Wu, J.; Xue, Y.; Yan, X.; Yan, W. S.; Cheng, Q. M.; Xie, Y., Co3O4 nanocrystals on single-walled carbon nanotubes as a highly efficient oxygen-evolving catalyst. *Nano Research* **2012,** *5* (8), 521-530.

5. Zhao, Y. F.; Chen, S. Q.; Sun, B.; Su, D. W.; Huang, X. D.; Liu, H.; Yan, Y. M.; Sun, K. N.; Wang, G. X., Graphene-Co3O4 nanocomposite as electrocatalyst with high performance for oxygen evolution reaction. *Scientific Reports* **2015,** *5,* 7629.

6. Mao, S.; Wen, Z. H.; Huang, T. Z.; Hou, Y.; Chen, J. H., High-performance bi-functional electrocatalysts of 3D crumpled graphene-cobalt oxide nanohybrids for oxygen reduction and evolution reactions. *Energy & Environmental Science* **2014,** *7* (2), 609-616.

7. Tong, Y.; Chen, P.; Zhou, T.; Xu, K.; Chu, W.; Wu, C.; Xie, Y., A Bifunctional Hybrid Electrocatalyst for Oxygen Reduction and Evolution: Cobalt Oxide Nanoparticles Strongly Coupled to B,N-Decorated Graphene. *Angew Chem Int Ed Engl* **2017,** *56* (25), 7121-7125.

8. Wang, H.; Dai, H., Strongly coupled inorganic-nano-carbon hybrid materials for energy storage. *Chem. Soc. Rev.* **2013,** *42* (7), 3088-3113.

9. Liang, Y.; Li, Y.; Wang, H.; Dai, H., Strongly Coupled Inorganic/Nanocarbon Hybrid Materials for Advanced Electrocatalysis. *J. Am. Chem. Soc.* **2013,** *135* (6), 2013-2036.

10. Liang, Y.; Wang, H.; Diao, P.; Chang, W.; Hong, G.; Li, Y.; Gong, M.; Xie, L.; Zhou, J.; Wang, J.; Regier, T. Z.; Wei, F.; Dai, H., Oxygen Reduction Electrocatalyst Based on Strongly

Coupled Cobalt Oxide Nanocrystals and Carbon Nanotubes. *J. Am. Chem. Soc.* **2012,** *134* (38), 15849-15857.

11. Liang, Y.; Li, Y.; Wang, H.; Zhou, J.; Wang, J.; Regier, T.; Dai, H., Co(3)O(4) nanocrystals on graphene as a synergistic catalyst for oxygen reduction reaction. *Nat Mater* **2011,** *10* (10), 780-6.

12. Long, X.; Li, J. K.; Xiao, S.; Yan, K. Y.; Wang, Z. L.; Chen, H. N.; Yang, S. H., A Strongly Coupled Graphene and FeNi Double Hydroxide Hybrid as an Excellent Electrocatalyst for the Oxygen Evolution Reaction. *Angew. Chem.-Int. Edit.* **2014,** *53* (29), 7584-7588.

13. Zhao, Q.; Yan, Z.; Chen, C.; Chen, J., Spinels: Controlled Preparation, Oxygen Reduction/Evolution Reaction Application, and Beyond. *Chem. Rev.* **2017,** *117* (15), 10121-10211.

14. Gupta, S.; Kellogg, W.; Xu, H.; Liu, X.; Cho, J.; Wu, G., Bifunctional Perovskite Oxide Catalysts for Oxygen Reduction and Evolution in Alkaline Media. *Chemistry-an Asian Journal* **2016,** *11* (1), 10-21.

15. Yang, J.; Liu, H. W.; Martens, W. N.; Frost, R. L., Synthesis and Characterization of Cobalt Hydroxide, Cobalt Oxyhydroxide, and Cobalt Oxide Nanodiscs. *J. Phys. Chem. C* **2010,** *114* (1), 111-119.

16. Burke, M. S.; Kast, M. G.; Trotochaud, L.; Smith, A. M.; Boettcher, S. W., Cobalt-iron (oxy)hydroxide oxygen evolution electrocatalysts: the role of structure and composition on activity, stability, and mechanism. *J Am Chem Soc* **2015,** *137* (10), 3638-48.

17. Ye, Y.-J.; Zhang, N.; Liu, X.-X., Amorphous NiFe(oxy)hydroxide nanosheet integrated partially exfoliated graphite foil for high efficiency oxygen evolution reaction. *Journal of Materials Chemistry A* **2017,** *5* (46), 24208-24216.

18. Zhou, J.; Wang, Y.; Su, X.; Gu, S.; Liu, R.; Huang, Y.; Yan, S.; Li, J.; Zhang, S., Electrochemically accessing ultrathin Co (oxy)-hydroxide nanosheets and operando identifying their active phase for the oxygen evolution reaction. *Energy & Environmental Science* **2019**, *12*, 739-746.

19. Zhou, Q.; Chen, Y.; Zhao, G.; Lin, Y.; Yu, Z.; Xu, X.; Wang, X.; Liu, H. K.; Sun, W.; Dou, S. X., Active-Site-Enriched Iron-Doped Nickel/Cobalt Hydroxide Nanosheets for Enhanced Oxygen Evolution Reaction. *ACS Catalysis* **2018,** *8* (6), 5382-5390.

20. Liu, R.; Wang, Y.; Liu, D.; Zou, Y.; Wang, S., Water-Plasma-Enabled Exfoliation of Ultrathin Layered Double Hydroxide Nanosheets with Multivacancies for Water Oxidation. *Adv Mater* **2017,** *29* (30), 1701546.

21. Zhao, Z.; Wu, H.; He, H.; Xu, X.; Jin, Y., A High-Performance Binary Ni–Co Hydroxide-based Water Oxidation Electrode with Three-Dimensional Coaxial Nanotube Array Structure. *Adv. Func. Mater.* **2014,** *24* (29), 4698-4705.

22. Ye, R.; del Angel-Vicente, P.; Liu, Y.; Arellano-Jimenez, M. J.; Peng, Z.; Wang, T.; Li, Y.; Yakobson, B. I.; Wei, S.-H.; Yacaman, M. J.; Tour, J. M., High-Performance Hydrogen Evolution from MoS2(1–x)P x Solid Solution. *Adv. Mater.* **2016,** *28* (7), 1427-1432.

23. Xia, C.; Jiang, Q.; Zhao, C.; Hedhili, M. N.; Alshareef, H. N., Selenide-Based Electrocatalysts and Scaffolds for Water Oxidation Applications. *Adv Mater* **2016,** *28* (1), 77-85.

24. Kuang, P. Y.; Zhu, B. C.; Li, Y. L.; Liu, H. B.; Yu, J. G.; Fan, K., Graphdiyne: a superior carbon additive to boost the activity of water oxidation catalysts. *Nanoscale Horizons* **2018,** *3* (3), 317-326.

25. Yang, J.; Park, S.; Choi, K. y.; Park, H.-S.; Cho, Y.-G.; Ko, H.; Song, H.-K., Activity-Durability Coincidence of Oxygen Evolution Reaction in the Presence of Carbon Corrosion: Case Study of MnCo2O4 Spinel with Carbon Black. *ACS Sustainable Chemistry & Engineering* **2018,** *6* (8), 9566-9571.

26. Wang, W.; Luo, J.; Chen, S., Carbon oxidation reactions could misguide the evaluation of carbon black-based oxygen-evolution electrocatalysts. *Chem Commun (Camb)* **2017,** *53* (84), 11556-11559.

27. Geiger, S.; Kasian, O.; Mingers, A. M.; Nicley, S. S.; Haenen, K.; Mayrhofer, K. J. J.; Cherevko, S., Catalyst Stability Benchmarking for the Oxygen Evolution Reaction: The Importance of Backing Electrode Material and Dissolution in Accelerated Aging Studies. *ChemSusChem* **2017**, *10*, 4140-4143.

28. Sun, H.; Xu, X.; Yan, Z.; Chen, X.; Jiao, L.; Cheng, F.; Chen, J., Superhydrophilic amorphous Co–B–P nanosheet electrocatalysts with Pt-like activity and durability for the hydrogen evolution reaction. *Journal of Materials Chemistry A* **2018,** *6* (44), 22062-22069.

29. Fan, J.; Chen, Z.; Shi, H.; Zhao, G., In situ grown, self-supported iron-cobalt-nickel alloy amorphous oxide nanosheets with low overpotential toward water oxidation. *Chem Commun* **2016,** *52* (23), 4290-4293.

30. Schäfer, H.; Sadaf, S.; Walder, L.; Kuepper, K.; Dinklage, S.; Wollschläger, J.; Schneider, L.; Steinhart, M.; Hardege, J.; Daum, D., Stainless steel made to rust: a robust water-splitting catalyst with benchmark characteristics. *Energy & Environmental Science* **2015,** *8* (9), 2685-2697.

31. Schäfer, H.; Chevrier, D. M.; Zhang, P.; Stangl, J.; Müller-Buschbaum, K.; Hardege, J. D.; Kuepper, K.; Wollschläger, J.; Krupp, U.; Dühnen, S.; Steinhart, M.; Walder, L.; Sadaf, S.; Schmidt, M., Electro-Oxidation of Ni42 Steel: A Highly Active Bifunctional Electrocatalyst. *Adv. Func. Mater.* **2016,** *26* (35), 6402-6417.

32. Schäfer, H.; Chatenet, M., Steel: The Resurrection of a Forgotten Water-Splitting Catalyst. *ACS Energy Letters* **2018,** *3* (3), 574-591.

33. Dong, W. J.; Song, Y. J.; Yoon, H.; Jung, G. H.; Kim, K.; Kim, S.; Lee, J.-L., Monolithic Photoassisted Water Splitting Device Using Anodized Ni-Fe Oxygen Evolution Catalytic Substrate. *Adv. Energy Mater.* **2017,** *7* (19), 1700659.

34. Chuah, X.-F.; Hsieh, C.-T.; Huang, C.-L.; Senthil Raja, D.; Lin, H.-W.; Lu, S.-Y., In-Situ Grown, Passivator-Modulated Anodization Derived Synergistically Well-Mixed Ni–Fe Oxides from Ni Foam as High-Performance Oxygen Evolution Reaction Electrocatalyst. *ACS Applied Energy Materials* **2018,** *2* (1), 743-753.

35. Park, H.; Park, I. J.; Lee, M. G.; Kwon, K. C.; Hong, S. P.; Kim, D. H.; Lee, S. A.; Lee, T. H.; Kim, C.; Moon, C. W.; Son, D. Y.; Jung, G. H.; Yang, H. S.; Lee, J. R.; Lee, J.; Park, N. G.; Kim, S. Y.; Kim, J. Y.; Jang, H. W., Water Splitting Exceeding 17% Solar-to-Hydrogen Conversion Efficiency Using Solution-Processed Ni-Based Electrocatalysts and Perovskite/Si Tandem Solar Cell. *ACS Appl Mater Interfaces* **2019,** *11* (37), 33835-33843.

36. Wang, L.; Zhang, G.; Liu, Y.; Li, W.; Lu, W.; Huang, H., Facile synthesis of a mechanically robust and highly porous NiO film with excellent electrocatalytic activity towards methanol oxidation. *Nanoscale* **2016,** *8* (21), 11256-63.

37. Zhang, G.; Li, W.; Xie, K.; Yu, F.; Huang, H., A One-Step and Binder-Free Method to Fabricate Hierarchical Nickel-Based Supercapacitor Electrodes with Excellent Performance. *Adv. Func. Mater.* **2013,** *23* (29), 3675-3681.

38. Jin, M.; Zhang, G.; Yu, F.; Li, W.; Lu, W.; Huang, H., Sponge-like Ni(OH)2-NiF2 composite film with excellent electrochemical performance. *Phys Chem Chem Phys* **2013,** *15* (5), 1601-1605.

39. Shrestha, N. K.; Yang, M.; Schmuki, P., Self-Ordered Nanoporous Nickel Oxide/Fluoride Composite Film with Strong Electrochromic Contrast. *Electrochemical and Solid-State Letters* **2010,** *13* (8), C21.

40. Lasia, A.; Rami, A., Kinetics of hydrogen evolution on nickel electrodes. *Journal of Electroanalytical Chemistry and Interfacial Electrochemistry* **1990,** *294* (1), 123-141.

41. McCrory, C. C.; Jung, S.; Peters, J. C.; Jaramillo, T. F., Benchmarking heterogeneous electrocatalysts for the oxygen evolution reaction. *J Am Chem Soc* **2013,** *135* (45), 16977-87.

42. Ebihara, K.; Takahashi, H.; Nagayama, M., Structure and density of anodic oxide films formed on aluminum in oxalic acid solutions *J. Surf. Finish. Soc. Jpn.* **1983,** *35* (4), 548-553.

43. Yoriya, S.; Grimes, C. A., Self-Assembled TiO2 Nanotube Arrays by Anodization of Titanium in Diethylene Glycol: Approach to Extended Pore Widening. *Langmuir* **2010,** *26* (1), 417-420.

44. Liang, K.; Guo, L.; Marcus, K.; Zhang, S.; Yang, Z.; Perea, D. E.; Zhou, L.; Du, Y.; Yang, Y., Overall Water Splitting with Room-Temperature Synthesized NiFe Oxyfluoride Nanoporous Films. *ACS Catalysis* **2017,** *7* (12), 8406-8412.

45. Shen, J.; Wang, M.; Zhao, L.; Jiang, J.; Liu, H.; Liu, J., Self-Supported Stainless Steel Nanocone Array Coated with a Layer of Ni-Fe Oxides/(Oxy)hydroxides as a Highly Active and Robust Electrode for Water Oxidation. *ACS Appl Mater Interfaces* **2018,** *10* (10), 8786-8796.

46. Lei, L.; Huang, D.; Zhou, C.; Chen, S.; Yan, X.; Li, Z.; Wang, W., Demystifying the active roles of NiFe-based oxides/(oxy)hydroxides for electrochemical water splitting under alkaline conditions. *Coord. Chem. Rev.* **2020,** *408,* 213177.

47. Lorenz, P.; Finster, J.; Wendt, G.; Salyn, J. V.; Zumadilov, E. K.; Nefedov, V. I., ESCA INVESTIGATIONS OF SOME NIO-SIO2 AND NIO-AL2O3-SIO2 CATALYSTS. *J. Electron Spectrosc. Relat. Phenom.* **1979,** *16* (4), 267-276.

48. Lochel, B. P.; Strehblow, H. H., BREAKDOWN OF PASSIVITY OF NICKEL BY FLUORIDE .2. SURFACE ANALYTICAL STUDIES. *J. Electrochem. Soc.* **1984,** *131* (4), 713-723.

49. Allen, G. C.; Curtis, M. T.; Hooper, A. J.; Tucker, P. M., X-RAY PHOTOELECTRON-SPECTROSCOPY OF IRON-OXYGEN SYSTEMS. *J. Chem. Soc.-Dalton Trans.* **1974,** (14), 1525-1530.

50. Li, J.; Aslam, M. K.; Chen, C., One-Pot Hydrothermal Synthesis of Porous α-Ni(OH)2/C Composites and Its Application in Ni/Zn Alkaline Rechargeable Battery. *J. Electrochem. Soc.* **2018,** *165* (5), A910-A917.

51. Pei, C.; Gu, Y.; Liu, Z.; Yu, X.; Feng, L., Fluoridated Iron-Nickel Layered Double Hydroxide for Enhanced Performance in the Oxygen Evolution Reaction. *ChemSusChem* **2019,** *12* (16), 3849-3855.

TOC

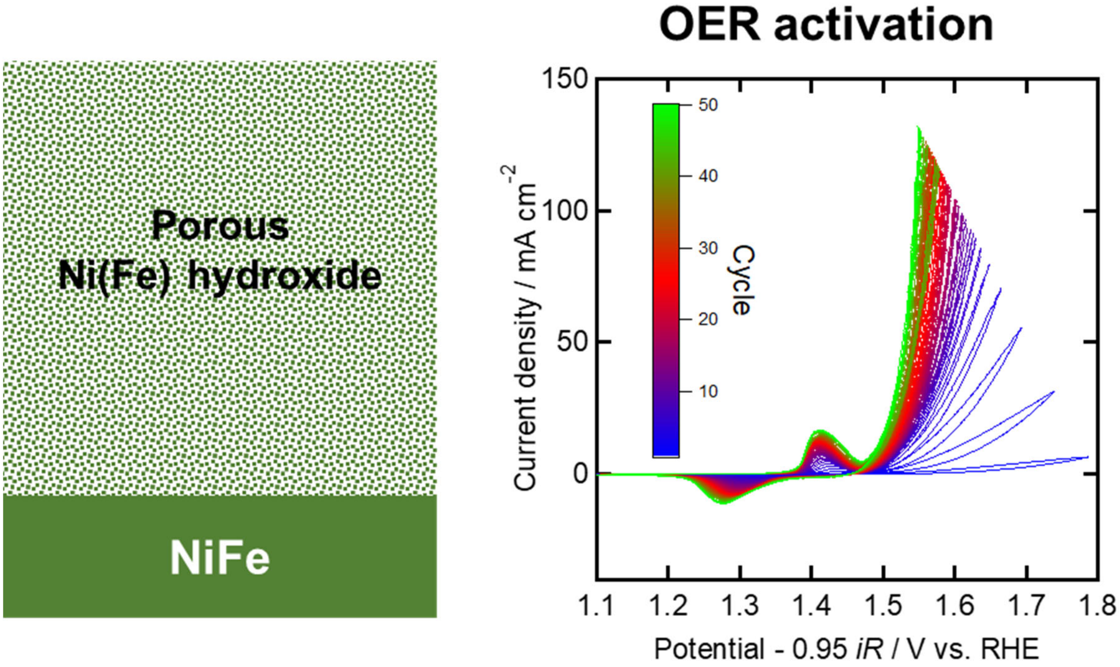
Porous
Ni(Fe) hydroxide
NiFe
OER activation
Current density / mA cm^{-2}
Potential - 0.95 *iR* / V vs. RHE
150
100
50
0
1.1
1.2
1.3
1.4
1.5
1.6
1.7
1.8
Cycle
50
40
30
20
10